# Microwave Synthesis of Classically Immiscible Rhodium–Silver and Rhodium–Gold Alloy Nanoparticles: Highly Active Hydrogenation Catalysts

Stephany García, Liang Zhang, Graham W. Piburn, Graeme Henkelman,* and Simon M. Humphrey*

Department of Chemistry, The University of Texas at Austin, Welch Hall 2.204, 105 East 24th Street Stop A5300, Austin, Texas 78712-1224, United States

ABSTRACT
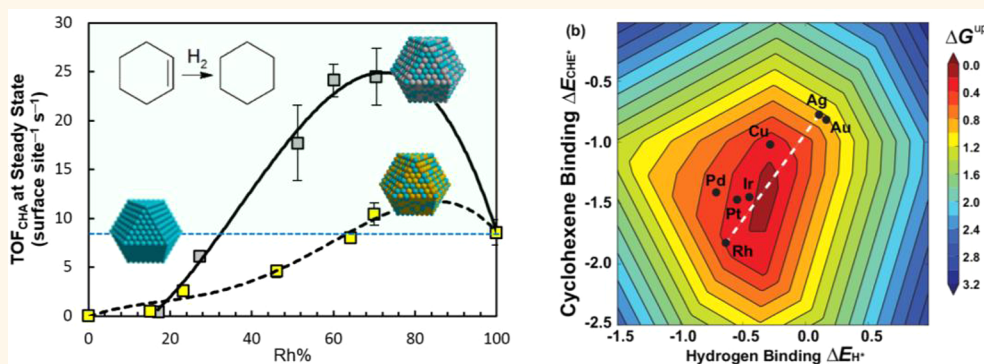
Noble metal alloys are important in large-scale catalytic processes. Alloying facilitates fine-tuning of catalytic properties *via* synergistic interactions between metals. It also allows for dilution of scarce and expensive metals using comparatively earth-abundant metals. RhAg and RhAu are classically considered to be immiscible metals. We show here that stable RhM (M = Ag, Au) nanoparticles with randomly alloyed structures and broadly tunable Rh:M ratios can be prepared using a microwave-assisted method. The alloyed nanostructures with optimized Rh:M compositions are significantly more active as hydrogenation catalysts than Rh itself: Rh is more dilute *and* more reactive when alloyed with Ag or Au, even though the latter are both catalytically inactive for hydrogenation. Theoretical modeling predicts that the observed catalytic enhancement is due to few-atom surface ensemble effects in which the overall reaction energy profile for alkene hydrogenation is optimized due to Rh–M *d*-band intermixing.

KEYWORDS: alloy nanoparticles · microwave synthesis · heterogeneous catalysis · immiscible alloys · density functional theory (DFT) · hydrogenation

Rapid, efficient, and scalable methods for the preparation of noble metal nanoparticle (NP) catalysts with defined structures and novel compositions are of great interest due to their potential applications in a broad range of industrially important processes.[1–5] Compared to classical colloidal heterogeneous catalysts, NPs provide higher surface area-to-volume ratios, which results in enhanced overall catalytic activities.[6–9] Fine control over nanoparticle morphology (surface structure) has also been shown to induce superior catalytic reactivity and selectivity.[7,10,11] It is also possible to discover new and potentially useful compositions of matter on the nanoscale, because mixtures of elements that are thermodynamically unstable in the bulk may actually become stable (or metastable) as a result of quantum size-confinement effects.[12–14]

Well-defined heterometallic nanostructures are of particular current interest because synergistic effects between metal atoms of different elements can result in enhancement of the catalytic properties by tuning the average binding energy of the NPs surface.[15–18] Multimetallic NPs also provide a convenient means to reduce the total amount of the rarest and most expensive metal *via* dilution with readily available,

and potentially catalytically inactive metals. Pertinent examples include core—shell NPs, which consist of thin shells of noble metals supported around cores of inexpensive materials;[19−21] the cores may also impart advantageous secondary properties (*e.g.*, ferromagnetic cores to enable NP recovery/separation,[22−24] or strain effects induced at the core—shell interface).[25,26] NPs with ordered intermetallic or randomly alloyed structures that consist of different metallic elements are also highly desirable: *d*-band intermixing between individual atoms allows for broad tuning of the chemical reactivity of the NP surface.[27,28] In essence, the reactivity of metal 'A' can be enhanced for a specific catalytic purpose by dilution with metal 'B', in the formation of an A_xB_{1-x} alloy.

The chemistry and catalytic behavior of bulk metallic alloys has been extensively studied, and is well understood.[29] Bimetallic alloys are presently utilized in large-scale industrial processes in both bulk and NP forms.[13,30] However, the application of bimetallic alloys in catalysis remains limited to combinations of metals that are miscible.[31] All metals can be mixed at high temperature, but many are deemed to be immiscible; phase segregation occurs upon cooling because alloy phases are unstable with respect to the pure metals. RhAg and RhAu alloys display this behavior. The phase diagrams for these alloys predict no regions of stability below 2177 or 2139 K and 1.0 atm, respectively.[32] For this reason, almost nothing is known about their chemical properties.[33−35] However, they would be of particular interest in catalysis since Rh is vital in a wide range of catalytic processes, but it is scarce and expensive. Meanwhile, Ag and Au are much more abundant. Ag is also inexpensive, but is not industrially as useful in pure form due to its inherent unreactivity.

We show here that a novel microwave-assisted technique enables the simple, programmable preparation of stable RhAg and RhAu alloy NPs with broadly tunable compositions. Application of the RhM (M = Ag or Au) NPs in model hydrogenation catalysis studies show that alloys with optimal compositions are as much as three times more reactive that pure Rh NPs under identical conditions: Rh becomes more reactive when diluted in alloys with Ag or Au, even though the latter metals are catalytically inactive for hydrogenation. We also present theoretical modeling studies that explain the observed increase in reactivity of the RhM alloy NPs, by describing how the average H-binding energy is modulated as a function of specific NP surface structure.

RESULTS AND DISCUSSION

We have previously demonstrated the beneficial effects of microwave irradiation (μwI) in the formation of monometallic noble metal nanoparticles of Rh, Pd and Pt.[36] Under μwI, NP nucleation from a supersaturated solution of metal ions occurs much more rapidly,

and more uniformly compared to analogous reactions under conventional (convective) heating. This is ascribed to the presence of nanosized "hotspots"[36] that are generated by strong rotational coupling of metal ions and polar solvents to μwI. Hotspots can be very much hotter than the bulk solvent temperature, thus providing favorable zones for NP nucleation. In comparison to conventionally prepared NPs, μwI also generates fewer, larger nucleates that are more highly crystalline and homogeneous. Seeding is effectively instantaneous under μwI; NP ripening is not observed after reaction times as short as 20 s. Addition of further metal precursor to the preformed seeds under μwI promotes selective growth to give larger NPs with defined size and surface structure.[36] The technique has also been applied to prepare core—shell species, whereby seed NPs consisting of catalytically inactive metals such as Ag or Au can be coated with thin (2−8 monolayer) shells of the desired catalytic metals in an atom-efficient manner.[21]

To the best of our knowledge, there has only been two previous reports of the formation of RhAu alloy NPs,[33,34] and one report of RhAg alloy NPs,[35] both obtained by conventional synthesis methods. The catalytic properties of these bimetallic MNPs have remained completely unexplored until now. We were able to successfully formulate a simple, reproducible μwI-assisted method to prepare defined alloy NPs of composition Rh_xM_{100-x}, where *x* is broadly tunable in the range 15−70, based on the molar ratios of metal precursors employed. The alloy NPs were synthesized at 150 °C under μwI using a simple polyol method that utilized ethylene glycol as both reducing agent and reaction medium, in addition to secondary reductants and excess poly(*N*-vinylpyrrolidone) (PVP) as a stabilizing agent. In a typical synthesis, precursor solutions of $RhCl_3$ and either $HAuCl_4$ or $AgNO_3$ were simultaneously injected into preheated solvent. The rate of addition was carefully controlled by means of syringe pumps with programmed addition profiles that optimize NP nucleation and growth phases (see Experimental Section and Supporting Information for full details).

We attempted to prepare RhM NPs with compositions of 3:1, 2:1, 1:1, 1:2 and 1:3, based on the molar ratios of metal precursors employed. The actual resulting metal compositions, Rh_xM_{100-x}, were determined by Inductively-Coupled Plasma Mass Spectrometry (ICP-MS). X-ray Photoelectron Spectroscopy (XPS) and Energy-Dispersive X-ray analysis (EDX) were also employed to check the compositions assumed from ICP-MS data; in all instances, these were in close agreement (Tables 1 and 2). Representative transmission electron microscopy (TEM) images of Rh_xAg_{100-x} NPs (*x* = 17−70) revealed a majority of truncated cubic and cuboctahedral NPs with *pseudo*-Gaussian size distributions (Figure 1a). Under identical reaction conditions, the RhAgNP compositions were broadly tunable

TABLE 1. Analytical and Catalytic Parameters for the RhAg NPs

		EDS atom% (as- synthesized)		XPS atom% (as- synthesized)		XPS atom % (*post*-catalysis)		
	NP size (nm)	Rh	Ag	Rh	Ag	Rh	Ag	E_{act}(kJ mol^{-1})
Rh	12.1 ± 1.9	100	0	100	0	100	0	57.2
Rh$_{70}$Ag$_{30}$	6.0 ± 1.2	88	11	88	12	82	18	22.6
Rh$_{60}$Ag$_{40}$	5.0 ± 1.4	75	25	77	23	75	25	15.4
Rh$_{51}$Ag$_{49}$	6.8 ± 1.3	53	47	65	35	48	52	28.3
Rh$_{27}$Ag$_{73}$	6.3 ± 1.5	30	70	33	67	45	55	38.3
Rh$_{17}$Ag$_{83}$	4.3 ± 1.2	19	81	27	73	37	63	38.1
Ag	7.8 ± 1.5	0	100	0	100	0	100	-

TABLE 2. Analytical and Catalytic Parameters for the RhAu NPs

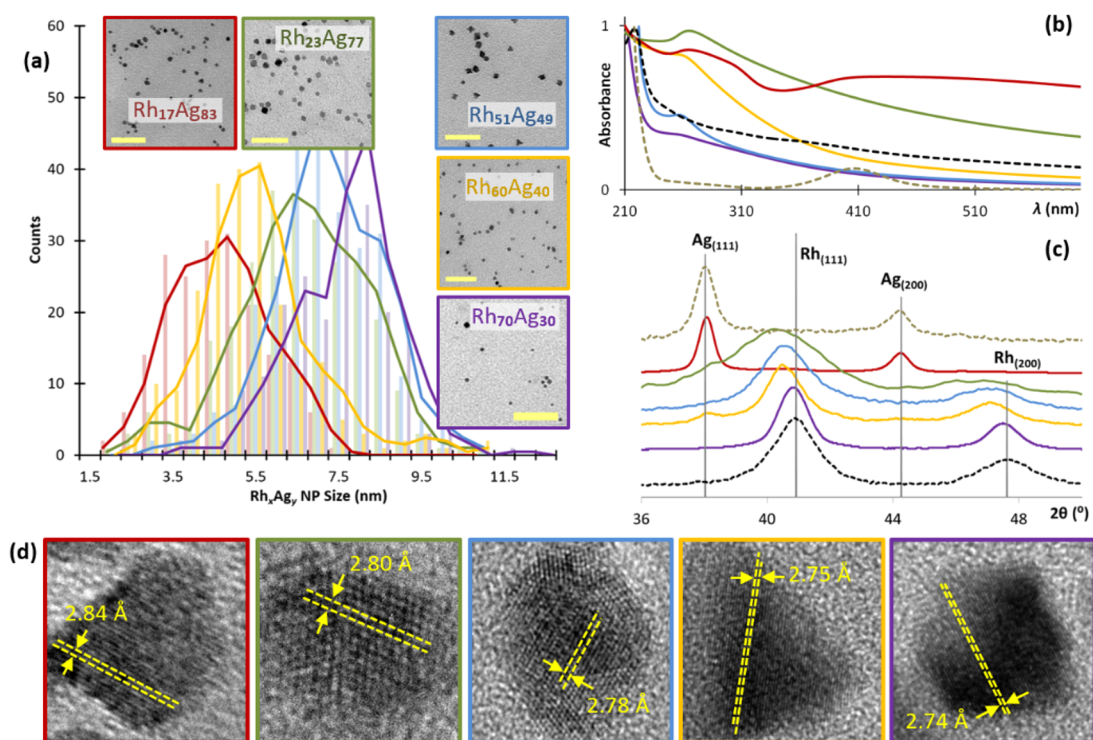|		EDS atom% (as- synthesized)		XPS atom% (as- synthesized)		XPS atom% (*post*-catalysis)		
	NP size (nm)	Rh	Au	Rh	Au	Rh	Au	E_{act} (kJ mol^{-1})
Rh	12.1 ± 1.9	100	0	100	0	100	0	57.2
Rh$_{70}$Au$_{30}$	3.3 ± 1.0	89	11	82	18	88	12	38.0
Rh$_{64}$Au$_{36}$	3.1 ± 1.2	68	32	71	29	70	30	44.5
Rh$_{45}$Au$_{54}$	2.4 ± 1.1	49	51	58	42	53	47	52.8
Rh$_{23}$Au$_{77}$	2.0 ± 0.8	32	68	30	70	38	62	45.9
Rh$_{15}$Au$_{85}$	4.3 ± 1.4	16	84	18	82	15	85	51.9
Au	5.6 ± 1.5	0	100	0	100	0	100	-

Figure 1. Analysis of μwI-RhAg NPs. (a) Size histograms and representative low-resolution TEM images (inset; scale bars = 50 nm). **(b)** UV−vis spectra for the five compositions of RhAg NPs studied along with the spectra for pure 12.1 nm Rh (black dashed line) and 7.8 nm Ag NPs (beige dashed line). **(c)** Expansion of the (111) region of the PXRD patterns; the standard index positions for the Ag(111) and Rh(111) reflections are shown in gray. **(d)** HRTEM images for individual NPs and the corresponding measured average lattice spacings (scale bars = 5 nm). Key: red = Rh$_{17}$Ag$_{83}$; green = Rh$_{23}$Ag$_{77}$; blue = Rh$_{51}$Ag$_{49}$; yellow = Rh$_{60}$Ag$_{40}$; purple = Rh$_{70}$Ag$_{30}$.

while the average NP size did not change significantly; all RhAgNPs were formed in the size range 5−6.8 nm.

Notably, alloyed RhAgNPs of all compositions were smaller than pure Rh or AgNPs that were obtained

under the same reaction conditions (Table 1). Also, when the same reactions were performed using conventional heating (and keeping all other parameters constant), we were only able to obtain highly polydisperse nanostructures, in which alloying was not evident (as determined by Powder X-ray Diffraction analysis (PXRD; Supporting Information Figures S25 ans S26)).

It is reasonable to assume that alloyed RhAgNPs prepared under μwI should be metastable on the nanoscale, based on their known immiscibility in the bulk. Indeed, control experiments were carried in which the alloyed NPs were systematically heated in 50 °C intervals, from 100 to 350 °C. The resulting PXRD analysis showed that the alloyed NPs began to undergo phase segregation at 300 °C (Supporting Information Figure S7). Furthermore, continuous growth experiments indicated the increasing presence of nonalloyed Ag and Rh metal as the diameter of the NPs approached *ca.* 20 nm (Supporting Information Figures S23 and S24).

UV/vis spectrophotometry of the RhAgNPs suspended in ethanol gave a unique, broad plasmon-enhanced absorption band at *ca.* 250–310 nm that is not observed in either pure Ag or Rh NPs of similar sizes (Figure 1b; beige and black dashed lines, respectively). This band was blue-shifted with increasing Rh content, which is consistent with the *d*-band center of Rh being lowered as the amount of Ag decreases and charge transfer from Rh to Ag subsides. The absorption band *ca.* 405 nm that is usually observed for AgNPs was absent for the alloyed NPs. PXRD analysis of the bulk RhAgNPs showed marked shifting of the lattice parameters due to alloying (Figure 1c). Rh and Ag each exhibit face-centered-cubic (FCC) lattice structures, but there is an approximate 7% lattice mismatch between them (Rh = 380; Ag = 408 pm). The intense (111) reflection was increasingly shifted to lower angle and became broader as the proportion of Ag was increased. Single NP studies also indicated randomly alloyed structures. High-resolution TEM imaging of RhAg NPs of varying compositions detected a mixture of {111} and {100} lattice planes. Measurement and comparison of the *d*-spacings corresponding to the {111} planes showed a continuous increase of the interatomic separation distance for increasingly Ag-rich NPs (Figure 1d). EDX of the bulk materials gave compositions in good agreement with that observed by ICP-MS (Table 1). EDX line scans of single NPs performed on $Rh_{17}Ag_{83}$, $Rh_{51}Ag_{49}$ and $Rh_{70}Ag_{30}$ samples showed comparable compositions to the bulk (Supporting Information Figures S8–S10). XPS is a *pseudo*-surface-specific technique because the penetration depth of the photons is limited to approximately 10 nm; in this instance, the RhAgNPs are encapsulated in PVP, which further limits the penetration depth of the X-ray source to a few monolayers.

Both metals were observed at or near the NP surfaces, with relative intensities that also show good agreement with ICP-MS and EDX values (Table 1). While this does not unequivocally confirm homogeneity of alloying throughout the RhAgNPs, it is an important confirmation of surface structure on which to base subsequent catalytic studies.

The complementary analyses described do clearly confirm that Rh and Ag could be effectively randomly alloyed on the nanoscale over a range of compositions. Rh_xAu_{100-x} NPs ($x = 23–70$) were prepared using the same μwI-assisted method (Figure 2). The RhAuNPs also displayed mostly cuboctahedral morphologies, but were significantly smaller than the RhAg NPs (average diameter = 2–4.3 nm; Figure 2a and Table 2). In all other respects, comprehensive analysis of the RhAuNPs conducted similarly to the RhAgNPs, provided equally satisfactory proof of random alloying across the composition range studied (Figure 2b–d and Supporting Information).

The RhM NPs of varying compositions were dispersed on amorphous silica by direct impregnation from water/ethanol suspensions, followed by drying in air at 70 °C. TEM studies of the composites showed that the NPs were spatially well-dispersed and retained their original size and morphology (Figure 3c,e). It should be noted that the catalysts were highly active in their as-synthesized state and did not require further activation *pre*-treatment, even when hydrogenation reactions were conducted at room temperature. This underlines the beneficial reactivity of the as-synthesized RhMNPs: NP restructuring or sintering that is often a problem caused by the need to employ harsh activation procedures was avoided in this instance. It has been previously suggested that μw-prepared NPs are more active than conventionally prepared analogues because less PVP is incorporated, possibly due to strong rotational coupling (excitation) of the polymer with the microwaves.[36]

Attempts to remove the capping polymer using solvents in which PVP is extremely soluble (ethanol, H_2O and tetrahydrofuran) resulted in agglomeration of the particles, even when supported on amorphous silica (Supporting Information Figures S18 and S19). The removal of the polymer was further confirmed by elemental analysis (Supporting Information Table S3).

The catalytic performances of the RhM NPs as a function of relative Rh:M compositions were assessed using cyclohexene hydrogenation as a convenient model reaction. All catalysis experiments were performed in the vapor-phase at 25.0 ± 0.1 °C using a single-pass configuration. A minimum of three catalytic experiments were performed under identical conditions utilizing different batches of the same composite material, in order to ensure reproducibility. Activity profiles for the as-synthesized catalysts (Figure 3a,b) are plotted with turnover frequencies (TOFs) that have been
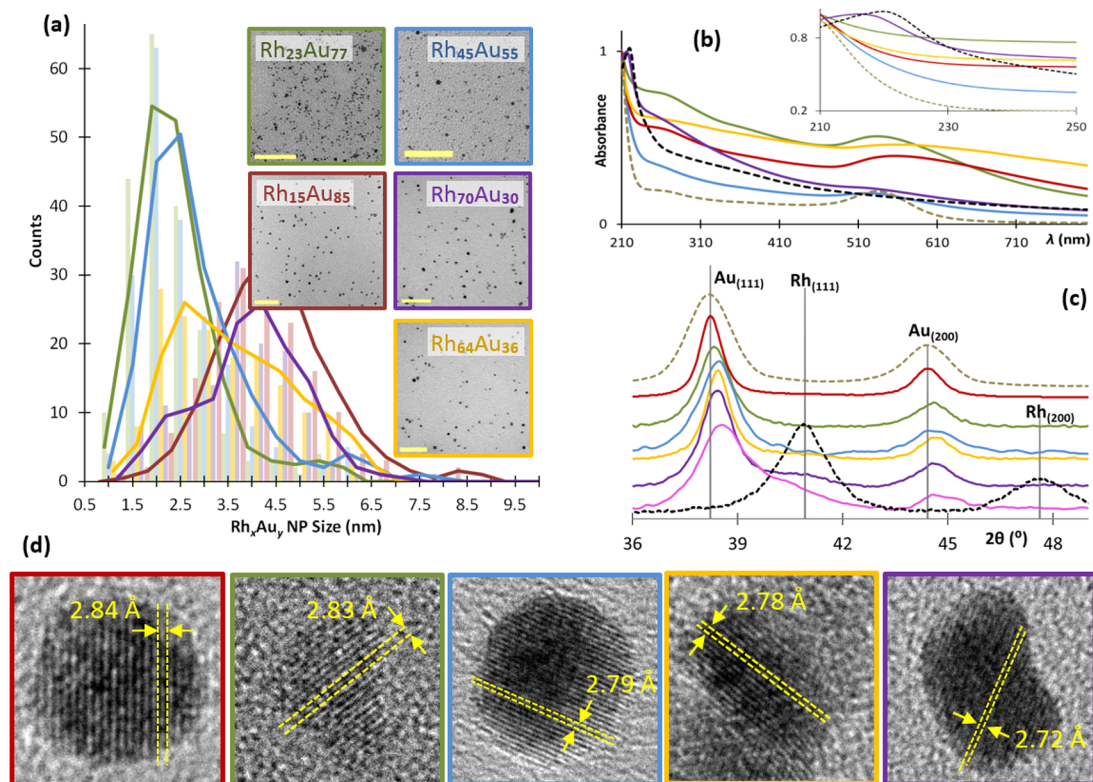
Figure 2. Analysis of RhAu NPs. (a) Size histographs and representative low-resolution TEM images (inset; scale bars = 50 nm). (b) UV−vis spectra for the five compositions of RhAu NPs studied along with the spectra for pure 12.1 nm Rh (black dashed line) and 5.6 nm Au NPs (beige dashed line). (c) Expansion of the (111) region of the PXRD patterns; the standard index positions for the Au(111) and Rh(111) reflections are shown in gray. (d) HRTEM images for individual NPs and the corresponding measured average lattice spacings (scale bars = 5 nm). Key: red = $Rh_{15}Au_{85}$; green = $Rh_{23}Au_{77}$; blue = $Rh_{45}Au_{55}$; yellow = $Rh_{64}Au_{36}$; purple = $Rh_{70}Au_{30}$.

normalized *per* surface site, by taking into account average NP dimensions and then using composition data obtained from XPS and ICP-MS experiments (see Supporting Information). First and foremost, it is directly apparent from the catalytic results obtained that RhM NPs with intermediate or slightly Rh-rich compositions were able to outperform pure Rh NPs. In the best case, it was determined that Rh-rich RhAg alloy NPs were three times more active catalysts than pure RhNPs. From a practical standpoint, this is an important result because *catalytically inactive Ag or Au can be utilized to dilute Rh and also to increase the apparent hydrogenation activity.* In general, the RhM alloy catalysts showed an initial, short induction period before activity gradually declined toward steady-state (Figure 3a,b). The catalysts remained stable at steady-state for up to 6 h. At longer times, some lowering in activity was observed (presumably due to the formation of carbonaceous species on the NP surfaces). However, initial catalytic activity was recovered upon recyclability testing, with only modest reduction in steady-state TOFs after the third reuse (Supporting Information Table S4).

Control studies were also performed to confirm that the increase in catalytic activity was due to the presence of preferential alloy compositions at the NP surfaces.

Three additional catalysts were prepared, each containing a 1:1 mixture of pure RhNPs and either AgNPs, AgClNPs or AuNPs, randomly dispersed together on silica. When these catalysts were tested under identical catalytic conditions, the normalized TOFs were the same as those observed for pure RhNPs (Supporting Information Figures S22, S45). This further confirmed that the catalytic enhancement was due to the alloy NPs rather than segregated metals, or trace amounts of AgClNPs.

Activation energies were measured for all catalysts by obtaining steady-state activity data between 5 and 30 °C (Tables 1 and 2 and Supporting Information). The measured activation energy for the most active catalyst ($Rh_{60}Ag_{40}$) was only 15.4 kJ mol^{-1} *versus* 57.2 kJ mol^{-1} for pure RhNPs. TEM images of the supported alloy NPs postcatalysis confirmed that the particles retained their shape and size during the catalytic process and were not agglomerated (Figure 3d,f and Supporting Information Figures S13−S17 and S38−S41). XPS and EDX analyses of the materials *post*-catalysis indicated that both metals were still present at the NP surfaces in proportions very similar to those measured in the fresh materials. Furthermore, the metals did not undergo segregation during hydrogenation catalysis under the model test conditions employed (Tables 1 and 2 and Supporting Information
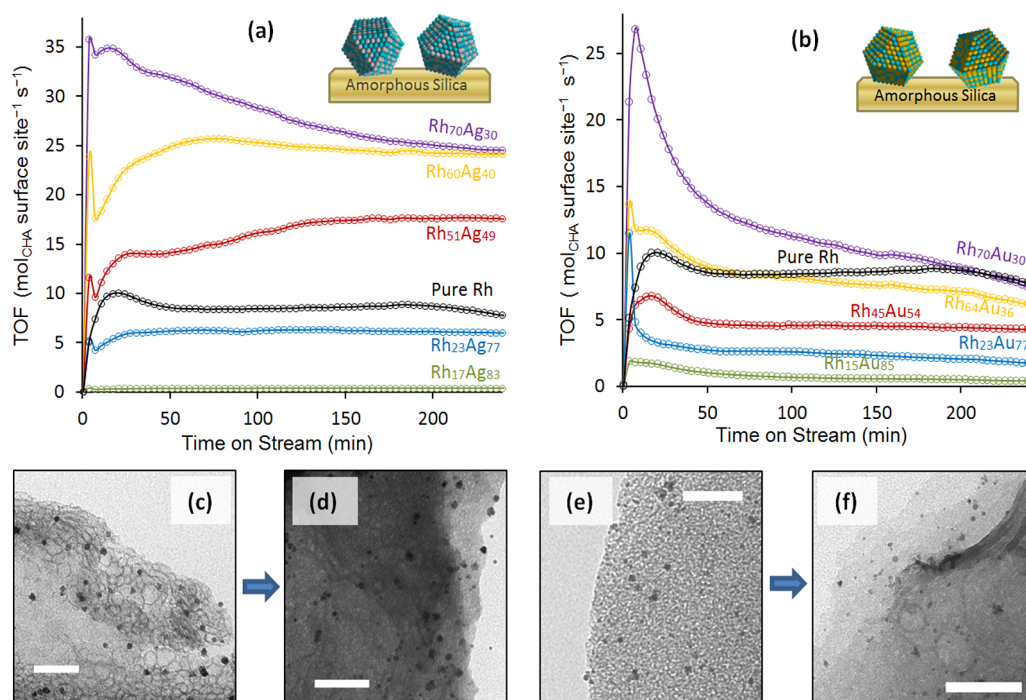
Figure 3. (a) Time-dependent TOF data for the vapor-phase hydrogenation of cyclohexene by the various RhAg NPs supported on silica, compared to Rh NPs. (b) Comparative data for the RhAu catalysts. (c) Representative TEM image of silica-supported Rh$_{70}$Ag$_{30}$ NPs before catalysis. (d) TEM image of the same catalyst material *post*-catalysis. (e) Representative TEM image of the silica-supported Rh$_{70}$Au$_{30}$ NP composite material before catalysis. (f) TEM image of the same material *post*-catalysis.
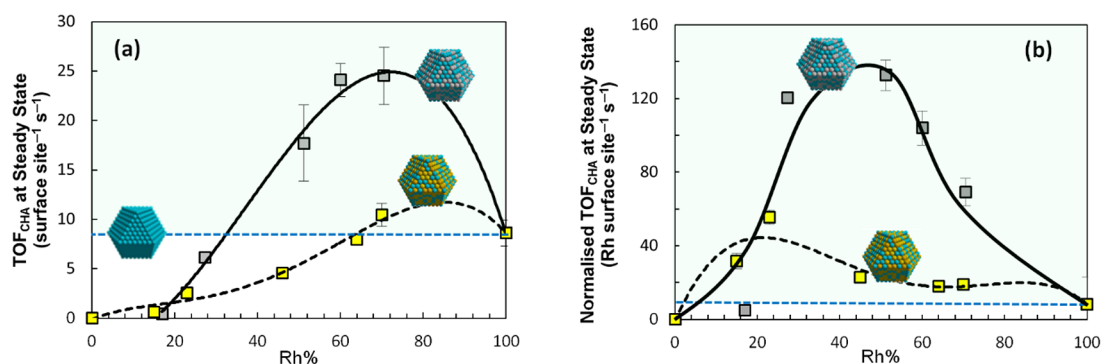

Figure 4. (a) A direct comparison of the steady-state rates of cyclohexene hydrogenation at 25.0 °C as a function of %Rh composition for the RhAg (gray) and RhAu (yellow) NPs *versus* pure Rh NPs (blue dashed line) prepared by μwI. (b) The same data when plotted using TOFs normalized for percent surface Rh.

Figures S11, S12, and S36−S37). Thus, any observed decrease in activity of the RhM NPs after the initial induction period cannot be attributed to phase segregation or enrichment of one particular metal at the NP surfaces and is more likely due to classical deactivation mechanisms (such as surface coking and/or restructuring of higher energy facets).

A direct comparison of the hydrogenation TOFs of supported RhM NPs as a function of composition (Figure 4a) clearly shows that NPs with optimized compositions out-performed pure RhNPs. This comparison does not even take into account the fact that Rh is diluted in the alloy NPs. From an absolute Rh atom economy standpoint, an alternative plot that

is normalized for Rh surface sites (assuming uniform concentration of Rh throughout the NPs) reveals that RhM NPs of all compositions above 20% Rh are more active than pure Rh NPs (Figure 4b and Supporting Information Figures S21, S42).

Determination of the reaction mechanism of cyclohexene (CHE) hydrogenation is key to understanding the volcano-like activity trends seen for the RhAu and RhAg alloys. Thus, we have used density functional theory (DFT) to study the hydrogenation reaction mechanism on a series of close-packed fcc(111) transition metal surfaces. The logic for focusing on the (111) facet is that it has the lowest surface energy for the elements of interest in this study.[37] The dispersion
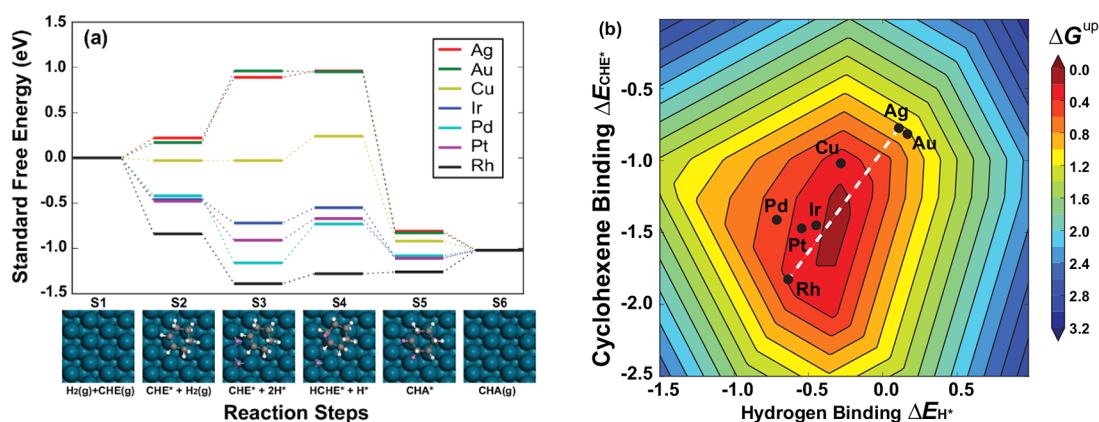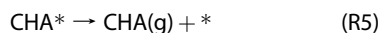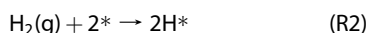
Figure 5. (a) Free energy profile for CHE hydrogenation with insets showing the reaction intermediates: blue spheres are metal atoms, gray are C, white are H from CHE, and pink are H from H_2. (b) Contour of ΔG^{up} as a function of the binding energy of CHE and H. A maximum activity can be achieved by alloying metals from different side of the volcano (*e.g.*, white dashed line).

energy term was treated using the method of Tkachenko and Scheffler.[38] The following elementary steps in the hydrogenation reaction are considered:

$$CHE(g) + * \rightarrow CHE* \tag{R1}$$

$$H_2(g) + 2* \rightarrow 2H* \tag{R2}$$

$$H* + CHE* \rightarrow HCHE* + * \tag{R3}$$

$$H* + HCHE* \rightarrow CHA* + * \tag{R4}$$

$$CHA* \rightarrow CHA(g) + * \tag{R5}$$

where CHE, HCHE, and CHA represent cyclohexene (C_6H_{10}), singly hydrogenated cyclohexene (C_6H_{11}), and cyclohexane (C_6H_{12}), respectively. The asterisk (*) denotes a binding site on the surface. Figure 5a shows the free energy profile of the above reaction on Ag, Au, Cu, Ir, Pd, Pt, and Rh under standard conditions ($T = 298.15$ K, $P = 1$ bar). Details of the free energy calculation can be found in the Supporting Information. The barriers of each elementary step are not included, however, this level of thermodynamic analysis has been demonstrated to capture the activity trends in previous studies.[39,40] As shown in Figure 5a, noble metals such as Ag and Au bind CHE and hydrogen too weakly so that the adsorption steps are endothermic. Rh on the other hand, binds them too strongly so that the hydrogenation and subsequent release of CHA from the surface are unfavorable.

The catalytic performance is estimated from the free energy that needs to be overcome along the reaction path, ΔG^{up}. Linear correlations between the binding energies of CHE, HCHE, and CHA (see Supporting Information Figure S50) allow for ΔG^{up} to be expressed simply in terms of the binding energies of H and CHE, as shown in Figure 5b. As can also be seen from the free energy diagram in Figure 5A, Ag/Au and Rh are located on opposite sides of the ΔG^{up} volcano. This picture

validates the observation of enhanced hydrogenation activity for the RhAu and RhAg alloy nanoparticles. As indicated from the white dashed line in Figure 5b, alloying Au and Ag to Rh weakens the binding of CHE and H, raising the free energy of S3−5 with respect to S6, and subsequently reducing ΔG^{up}. Another interesting finding from Figure 5b is that the binding of CHE and H are also correlated with each other, for the fcc(111) transition metal surfaces we investigated, which allows us to use the binding energy of hydrogen as a qualitative reactivity descriptor for the hydrogenation reaction in the following discussion.

From the above thermodynamic analysis, the peak of volcano is located near $\Delta E_{H*} = -0.4$ eV. Considering the large difference in reactants affinity between Ag/Au and Rh, it is important to decompose the hydrogen binding at different compositions into ensembles of binding sites.[41−43] For clarity, we will focus our discussion on the RhAg system in the main text; the RhAu system (which can be found in the Supporting Information) differs only in the quantitative values. Figure 6 shows that the average binding of H increases with Rh composition in the Ag/Rh alloy. For each intermediate alloy composition, the average binding energy (Figure 6; black line) is decomposed into individual histograms of binding sites. The target H binding $\Delta E_{H*} = -0.4$ eV is highlighted by the orange dashed line. Four sites can be distinguished from these data; these correspond to the four possible combinations of Ag and Rh atoms in each 3-fold hollow site, where H atoms can be adsorbed (Rh_3, Rh_2Ag_1, Rh_1Ag_2, and Ag_3; Figure 6, inset). The large disparity in binding energies at these different sites indicates that they should be considered separately, rather than as part of an average. Interestingly, the H binding energy of the Rh_3 and Rh_2Ag_1 sites increases with increasing Ag content, as compared to the pure Rh particle (red and blue dashed line in Figure 6, in contrast to the solid black overall trend), indicating
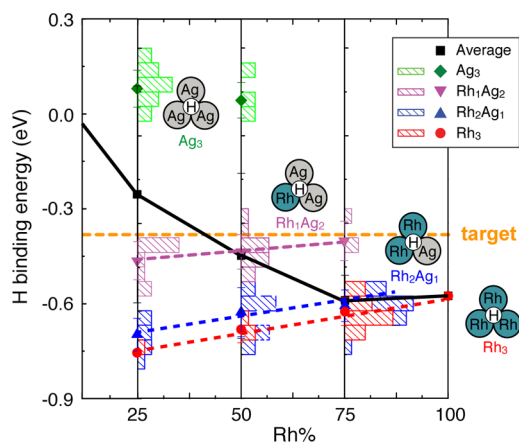
Figure 6. Decomposition of the average H binding energy into an ensemble of specific sites determined by the number of Ag *vs* Rh atoms at the binding site. The bars indicate the frequency of different binding energies at the three intermediate compositions, and the solid symbols indicate the average binding energy *per* site. Trends in the activity of the most active Rh-rich sites as a function of composition (red and blue dashed lines) are different from the overall trend (black solid line); the target H binding at about −0.4 eV is highlighted by the orange dashed line.

that H or CHE will overbind and saturate these Rh-rich sites. The Ag_3 site binds H too weakly to adsorb

reactants. The most active site, which is closest to the peak of the ΔG^{up} volcano, is the Rh_1Ag_2 site. As more Ag is alloyed to Rh, there is a higher ratio of Rh_1Ag_2 sites on the surface, until the surface is dominated by Ag_3 sites. On the other hand, we can also see that a higher Ag ratio increases the H binding of sites containing Rh, away from the target. The trade-off between these two effects results in the volcano-like hydrogenation activity trend of RhAg alloy nanoparticles.

CONCLUSIONS

A novel microwave-assisted solution-phase method allows for the simple and programmable preparation of unconventional NPs of RhAg and RhAu with randomly alloyed structures. The composition of the RhM NPs can be systematically varied to optimize their catalytic properties. The combined experimental and theoretical study presented here clearly shows that RhAg NPs in particular have great potential in heterogeneous catalysis. Particular ensembles at the bimetallic NP surfaces result in highly active sites that create an optimal balance between substrate binding and release, which are generated by dilution of Rh with Ag or Au.

EXPERIMENTAL SECTION

RhAg and RhAu alloy NPs of different compositions were synthesized using the same polyol reduction method. In all instances, poly(vinylpyrrolidone) (PVP; MW = 58K, 4.5−9.0 mol monomer/mol metal) was dissolved in ethylene glycol (20.0 cm^3) and the temperature was brought to 150 °C (±0.1 °C) using a MARS microwave reactor (CEM Corp.) operating with fiber-optic temperature feedback control, and magnetic stirring (1100 rpm) at ambient pressure. Metal precursors dissolved in the same solvent were then concomitantly injected into the reaction mixture at specific rates, controlled using a programmable dual syringe pump (WPI, Inc.) all while the reaction was still exposed to μwI. The reagents were delivered down utilizing 1.0 mm PTFE tubing, terminated 0.5 cm above the reaction mixture. See supporting content for a full schematic of the reaction apparatus (Supporting Information Scheme S1). Upon completion of a given reaction, the mixture was rapidly cooled by quenching in an ice−water bath. The resulting RhM alloy NPs were purified by initial precipitation with acetone and isolation by ultracentrifugation (5.5 krpm). Two cycles of redispersion in ethanol and reprecipitation with hexane followed by centrifugal isolation were then employed to remove excess PVP. The RhM NPs can be stored dry as an amorphous glass, or suspended in ethanol at room temperature.

Rh$_x$Ag$_{100−x}$ Alloys (x = 17−70). Prior to injection of the metal precursors, HCl (25.0 μM; 1.5−3.0 cm^3) in ethylene glycol was added to the hot glycol/PVP solution to enhance etching of Ag(0) clusters. Solutions of AgNO$_3$ and RhCl$_3$·xH$_2$O in ethylene glycol (5.0 cm^3) were then simultaneously added at a rate of 150 cm^3 h$^{−1}$. The relative molar amounts of each precursor were determined by the desired value of x for the Rh$_x$Ag$_{100−x}$ products; in all instances, the total molar amount of added metal was constant. See Supporting Information for further details (Table S5). The mixture was allowed to continue stirring under microwave irradiation at the same temperature for 30 min after completion of precursor addition. Following precipitation, the RhAg NPs were suspended in H$_2$O and washed

with NH$_4$OH (29.1% assay, 1.0 cm^3) to remove any residual AgCl NPs, using the method of Schuette *et al.*[44]

Rh$_x$Au$_{100−x}$ Alloys (x = 23−70). RhAu alloy NPs were synthesized using NaBH$_4$ (5 equiv per Au(III)) to aid in the reduction of Au(III). A single solution containing both RhCl$_3$·xH$_2$O and HAuCl$_4$·3H$_2$O dissolved in ethylene glycol (5.0 cm^3) was prepared. The relative molar amounts of each precursor were determined by the desired value of x for the desired Rh$_x$Au$_{100−x}$ products; see Supporting Information (Table S6). A total of 2.50 cm^3 of this solution was added to the hot glycol/PVP/NaBH$_4$ soluton at an initial rate of 300 cm^3 h$^{−1}$ to induce nucleation of RhAu seeds. The mixture was stirred at constant temperature for 30 min, after which time the remaining precursor solution was added at a rate of 20 cm^3 h$^{−1}$ to promote controlled overgrowth at the existing seeds. The RuAu NPs were further ripened at 150 °C for 30 min upon completion of the second addition phase.

Catalytic Studies. The catalysts were prepared by addition of precalcined SiO$_2$ (200 mg) to suspensions of 8−12 mg of PVP-capped RhAg and RhAu NPs in ethanol/H$_2$O (1:1). The slurries were sonicated (20 min), isolated by filtration, washed with ethanol/H$_2$O and dried at 70 °C. The resulting composites contained between 0.5 and 3.5 wt % of noble metals. For each catalytic study, a small amount of catalyst (5−15 mg) was diluted with acid-washed and calcined sand and loaded into a custom-made quartz U-tube, suspended above a D3-porosity frit. The sample was held constant at 25 °C using a water bath and circulator, and the entire reactor line (quartz, heated to 90 °C) was purged with the reactant gas mixture (H$_2$/He 1:1) for 30 min. Catalysis began with the introduction of cyclohexene vapor into the gas stream *via* an in-line saturator fitted with a fritted bubbler. The purity of cyclohexene substrate (Acros Organics, ≥99%) was verified prior to use by gas chromatography and ^{1}H and ^{13}C{^{1}H} NMR spectroscopy (Supporting Information Figures S43−S44). All data was obtained in real-time by automated pneumatically gated sampling of the exhaust stream into an HP Agilent 6890 GC fitted with Restex Stabiliwax 15 m column and tandem FID and TCD detectors. Activity and

turnover frequency values were obtained based on estimated surface area-to-volume ratios (by TEM). Activation energies were determined by collection of steady-state activity values at five temperatures (in the range 5–30 °C). See Supporting Information for further details including characterizing data for the catalysts pre- and post-catalysis, catalyst recyclability studies, and data analysis.

Computational Studies. Adsorbate binding energy calculations were performed with VASP using a 4 layer (3 × 3) slab model of a (111) facet.[45,46] Core electrons were described using the projector-augmented wave method.[47,48] Exchange-correlation energy was evaluated by generalized gradient approximation (GGA) using the Perdew–Wang 91 functional.[49] The kinetic energy cutoff for the plane-wave basis was set to 280 eV.[50] For each composition, 64 random binding sites were calculated to obtain the H-binding ensemble.

Conflict of Interest: The authors declare no competing financial interest.

Supporting Information Available: Deconvoluted XPS spectra for the RhM NPs; EDS line scan spectra for selected compositions; TEM and HRTEM images with corresponding EDS data for catalysts *pre-* and *post*-catalysis; Arrhenius plots used to obtain catalyst activation energies; additional cyclohexene hydrogenation TOF data including recyclability studies and for a 1:1 control mixture of pure Rh and AgNPs; additional PXRD data and TEM comparisons of products obtained using conventional heating; additional catalysis and computational method data. This material is available free of charge *via* the Internet at http://pubs.acs.org.

REFERENCES AND NOTES

1. Burda, C.; Chen, X.; Narayanan, R.; El-Sayed, M. A. Chemistry and Properties of Nanocrystals of Different Shapes. *Chem. Rev.* **2005**, *105*, 1025–1102.

2. Stratakis, M.; Garcia, H. Catalysis by Supported Gold Nanoparticles: Beyond Aerobic Oxidative Processes. *Chem. Rev.* **2012**, *112*, 4469–4506.

3. Gross, E.; Liu, J. H.-C.; Toste, F. D.; Somorjai, G. A. Control of Selectivity in Heterogeneous Catalysis by Tuning Nanoparticle Properties and Reactor Residence Time. *Nat. Chem.* **2012**, *4*, 947–952.

4. Bell, A. T. The Impact of Nanoscience on Heterogeneous Catalysis. *Science* **2003**, *299*, 1688–1691.

5. Heveling, J. Heterogeneous Catalytic Chemistry by Example of Industrial Applications. *J. Chem. Educ.* **2012**, *89*, 1530–1536.

6. Roucoux, A.; Schulz, J.; Patin, H. Reduced Transition Metal Colloids: A Novel Family of Reusable Catalysts? *Chem. Rev.* **2002**, *102*, 3757–3778.

7. Cuenya, B. R. Synthesis and Catalytic Properties of Metal Nanoparticles: Size, Shape, Support Composition and Oxidation State Effects. *Thin Solid Films* **2010**, *518*, 3127–3150.

8. He, J.; Ichinose, I.; Kunitake, T.; Nakao, A.; Shiraishi, Y.; Toshima, N. Facile Fabrication of Ag-Pd Bimetallic Nanoparticles in Ultrathin TiO$_2$-Gel Films: Nanoparticle Morphology and Catalytic Activity. *J. Am. Chem. Soc.* **2003**, *125*, 11034–11040.

9. Wang, C.; Daimon, H.; Lee, Y.; Kim, J.; Sun, S. Synthesis of Monodisperse Pt Nanocubes and their Enhanced Catalysis for Oxygen Reduction. *J. Am. Chem. Soc.* **2007**, *129*, 6974–6975.

10. Bratlie, K. M.; Lee, H.; Komvopoulos, K.; Yang, P.; Somorjai, G. A. Platinum Nanoparticle Shape Effects on benzene hydrogenation Selectivity. *Nano Lett.* **2007**, *7*, 3097–3101.

11. Narayanan, R.; El-Sayed, M. A. Shape-Dependent Catalytic Activity of Platinum Nanoparticles in Colloidal Solution. *Nano Lett.* **2004**, *4*, 1343–1348.

12. Hills, C. W.; Mack, N. H.; Nuzzo, R. G. The Size-Dependent Structural Phase Behaviors of Supported Bimetallic (Pt-Ru) Nanoparticles. *J. Phys. Chem. B* **2003**, *107*, 2626–2636.

13. Ferrando, R.; Jellinek, J.; Johnston, R. L. Nanoalloys: From Theory to Applications of Alloy Clusters and Nanoparticles. *Chem. Rev.* **2008**, *108*, 845–910.

14. Buhro, W. E.; Coliv, V. L. Semiconductor Nanocrystals: Shape Matters. *Nat. Mater.* **2003**, *2*, 138–139.

15. Liu, J.-H.; Wang, A.-Q.; Chi, Y.-S.; Lin, H.-P.; Mou, C.-Y. Synergistic Effect in an Au-Ag Alloy Nanocatalyst: CO Oxidation. *J. Phys. Chem. B* **2005**, *109*, 40–43.

16. Wang, D.; Villa, A.; Porta, F.; Prati, L.; Su, D. Bimetallic Gold/Palladium Alloy Nanoparticle Catalysts. *J. Phys. Chem. C* **2008**, *112*, 8617–8622.

17. Mott, D.; Luo, J.; Njoki, P. N.; Lin, Y.; Wang, L.; Zhong, C.-J. Synergistic Activity o Gold-Platinum Alloy Nanoparticle Catlaysts. *Catal. Today* **2007**, *122*, 378–385.

18. Zhang, L.; Iyyamperumal, R.; Yancey, D. F.; Crooks, R. M.; Henkelman, G. Design of Pt-Shell Nanoparticles with Alloy Cores for the Oxygen Reduction Reaction. *ACS Nano* **2013**, *7*, 9168–9172.

19. Chaudhuri, R. G.; Paria, S. Core/Shell Nanoparticles: Classes, Properties, Synthesis Mechanisms, Characterization, and Applications. *Chem. Rev.* **2012**, *112*, 2373–2433.

20. Zhang, J.; Lima, F. H. B.; Shao, M. H.; Sasaki, K.; Wang, J. X.; Hanson, J.; Adzic, R. R. Platinum Monolayer on Nonnoble Metal-Noble Metal Core-Shell Nanoparticle Electrocatalysts. *J. Phys. Chem. B* **2005**, *109*, 22701–22704.

21. Garcia, S.; Anderson, R. M.; Celio, H.; Dahal, N.; Dolocan, A.; Zhou, J.; Humphrey, S. M. Microwave Synthesis of Au-Rh Core-Shell Nanoparticles and Implications of the Shell Thickness in Hydrogenation Catalysis. *Chem. Commun.* **2013**, *49*, 4241–4243.

22. Yan, J.-M.; Zhang, X.-B.; Akita, T.; Haruta, M.; Xu, Q. One-Step Seeding Growth of magnetically Recyclable Au@Co Core-Shell Nanoparticles: Highly Efficient Catalyst for Hydrolytic Dehydrogenation of Ammonia Borane. *J. Am. Chem. Soc.* **2010**, *132*, 5326–5327.

23. Zeng, H.; Li, J.; Wang, Z. L.; Liu, J. P.; Sun, S. Bimagnetic Core/Shell FePt/Fe$_3$O$_4$ Nanoparticles. *Nano Lett.* **2004**, *4*, 187–190.

24. Zeng, H.; Sun, S.; Li, J.; Wang, Z. L.; Liu, J. P. Tailoring Magnetic Properties of Core/Shell Nanoparticles. *Appl. Phys. Lett.* **2004**, *85*, 792–794.

25. Strasser, P.; Koh, S.; Anniyev, T.; Greeley, J.; More, K.; Yu, C.; Liu, Z.; Kaya, S.; Nordlund, D.; Ogasawara, H.; *et al.* Lattice-Strain Control of the Activity in Dealloyed Core-Shell Fuel Cell Catalysts. *Nat. Chem.* **2010**, *2*, 454–460.

26. Mavrikakis, M.; Hammer, B.; Nørskov, J. K. Effect of Strain on the Reactivity of Metal Surfaces. *Phys. Rev. Lett.* **1998**, *81*, 2819–2822.

27. Yi, C. W.; Luo, K.; Wei, T.; Goodman, D. W. The Composition and Structure of Pd-Au Surfaces. *J. Phys. Chem. B* **2005**, *109*, 18535–18540.

28. Wang, W. H.; Dong, C.; Shek, C. H. Bulk Metallic Glasses. *Mater. Sci. Eng. R* **2004**, *44*, 45–89.

29. Kusada, K.; Kobayashi, H.; Ikeda, R.; Kubota, Y.; Takata, M.; Toh, S.; Yamamoto, T.; Matsumura, S.; Sumi, N.; Sato, K.; Nagaoka, K.; Kitagawa, H. Solid Solution Alloy Nanoparticles of Immiscible Pd and Ru Elements Neighboring on Rh: Changeover of the Thermodynamic Behavior for Hydrogen Storage and Enhanced CO-Oxidizing Ability. *J. Am. Chem. Soc.* **2014**, *136*, 1864–1871.

30. Thomas, J. M.; Johnson, B. F. G.; Raja, R.; Sankar, G.; Midgley, P. A. High-Performance Nanocatalysts for Single-Step Hydrogenations. *Acc. Chem. Res.* **2003**, *36*, 20–30.

31. Wang, F. E. In *Bonding Theory for Metals and Alloys*, 1st ed.; Elsevier B. V.: Amsterdam, 2005; pp 9–48.

32. Davies, R. H.; Dinsdale, A. T.; Gisby, J. A.; Robinson, J. A. J.; Martin, S. M. MTDATA—Thermodynamics and Phase Equilibrium Software from the National Physical Laboratory. *Calphad* **2002**, *26*, 229–271.

33. Essinger-Hileman, E. R.; DeCicco, D.; Bondi, J. F.; Schaak, R. E. Aqueous Room-Temperature Synthesis of Au-Rh, Au-Pt, Pt-Rh and Pd-Rh Alloy Nanoparticles: Fully Tunable Compositions Within the Miscibility Gaps. *J. Mater. Chem.* **2011**, *21*, 11599–11604.

34. Chantry, R. L.; Atanasov, I.; Siriwatcharapiboon, W.; Khanal, B. P.; Zubarev, E. R.; Horswell, S. L.; Johnston, R. L.; Li, Z. Y. An Atomistic View of the Interfacial Structures of AuRh and AuPd Nanorods. *Nanoscale* **2013**, *5*, 7452–7457.

35. Kusada, K.; Yamauchi, M.; Kobayashi, H.; Kitagawa, H.; Kubota, Y. Hydrogen Storage Properties. *J. Am. Chem. Soc.* **2010**, *132*, 15896–15898.

36. Dahal, N.; Garcia, S.; Zhou, J.; Humphrey, S. M. Beneficial Effects of Microwave-Assisted Heating *versus* Conventional Heating in Noble Metal Nanoparticle Synthesis. *ACS Nano* **2012**, *6*, 9433–9446.

37. Vitosa, L.; Rubana, A. V.; Skrivera, H. L.; Kollárb, J. The Surface Energy of Metals. *Surf. Sci.* **1998**, *411*, 186–202.

38. Tkatchenko, A.; Scheffler, M. Accurate Molecular van der Waals Interactions from Ground-State Electron Density and Free-Atom Reference Data. *Phys. Rev. Lett.* **2009**, *102*, 073005.

39. Rossmeisl, J.; Qu, Z. W.; Zhu, H.; Kroes, G. J.; Norskov, J. K. Electrolysis of Water on Oxide Surfaces. *J. Electroanal. Chem.* **2007**, *607*, 83–89.

40. Nørskov, J. K.; Rossmeisl, J.; Logadottir, A.; Lindqvist, L.; Kitchin, J. R.; Bligaard, T.; Jonsson, H. Origin of the Overpotential for Oxygen Reduction at a Fuel-Cell Cathode. *J. Phys. Chem. B* **2004**, *108*, 17886–17892.

41. Galema, S. A. Microwave Chemistry. *Chem. Soc. Rev.* **1997**, *26*, 233–238.

42. Maroun, F.; Ozanam, F.; Magnussen, O. M.; Behm, R. J. The Role of Atomic Ensembles in the Reactivity of Bimetallic Electroncatalysts. *Science* **2001**, *293*, 1811–1814.

43. Liu, P.; Norskøv, J. K. Ligand and Ensemble Effects in Adsorption on Alloy Surfaces. *Phys. Chem. Chem. Phys.* **2001**, *3*, 3814–3818.

44. Schuette, W. M.; Buhro, W. E. Silver Chloride as a Heterogeneous Nucleant for the Growth of Silver Nanowires. *ACS Nano* **2013**, *7*, 3844–3853.

45. Kresse, G. Dissociation and Sticking of H_2 on the Ni(111), (100), and (110) Susstrate. *Phys. Rev. B* **2000**, *62*, 8295–8305.

46. Kresse, G.; Hafner, J. First Principles Study of the Adsorption of Atomic H on Ni(111). *Surf. Sci.* **2000**, *459*, 287–302.

47. Blöchl, P. E. Projector Augmented-Wave Method. *Phys. Rev. B* **1994**, *50*, 17953–17979.

48. Kresse, G.; Joubert, D. From Ultrasoft Pseudopotentials to the Projector Augmented-Wave Method. *Phys. Rev. B* **1999**, *59*, 1758–1775.

49. Perdew, J. P.; Wang, Y. Accurate and Simple Analytic Representation of the Electron-Gas Correlation Energy. *Phys. Rev. B* **1992**, *45*, 13244–13249.

50. Hohenberg, P.; Kohn, W. Inhomogeneous Electron Gas. *Phys. Rev.* **1964**, *136*, B864–B887.